Journal of Catalysis **196,** 8–17 (2000)
doi:10.1006/jcat.2000.3024, available online at http://www.idealibrary.com on IDEAL®

Phase Transformations in Iron Fischer–Tropsch Catalysts during Temperature-Programmed Reduction

Yaming Jin[1] and Abhaya K. Datye[2]

Center for Microengineered Materials and Department of Chemical and Nuclear Engineering, University of New Mexico, Albuquerque, New Mexico 87131

Received December 1, 1999; revised August 4, 2000; accepted August 4, 2000

Temperature-programmed reduction using both carbon monoxide (CO-TPR) and hydrogen (H_2-TPR) was used to study the phase transformations in iron catalysts. High-resolution transmission electron microscopy (HRTEM) and X-ray diffraction (XRD) allowed us to follow the phase transformations in these iron catalysts during TPR. Two catalysts were used, a model supported catalyst with a nonporous silica support and a precipitated catalyst with no support. Under identical CO-TPR conditions, the supported and unsupported iron catalysts behaved very differently. For the supported catalyst, three stages of phase transformation could be identified: hematite to magnetite, magnetite to iron carbide, and in the third stage significant carbon deposition accompanying further carburization. No carbide formation or significant carbon deposition was observed in the unsupported Fe catalyst, due to the presence of S impurities in the unsupported catalyst. Most importantly, the results show that carbon deposition occurs in parallel with carbide formation, no carbon being seen in the catalyst that was not carbided. In these catalysts, copper facilitates the reduction of iron oxide, especially the transformation of hematite to magnetite. Segregation of copper from iron oxide causes the hematite to magnetite transformation to shift to higher temperatures. No interfacial Fe–SiO_2 phases could be detected during both CO-TPR and H_2-TPR. The major role of the silica support is to prevent the sintering of the Fe phases.

Key Words: **Fischer–Tropsch; Fe catalyst; temperature-programmed reduction; phase transformations.**

INTRODUCTION

The Fischer–Tropsch synthesis (FTS) for the production of liquid hydrocarbons from coal-based synthesis gas has been the subject of renewed interest for conversion of coal and natural gas to liquid fuels. The use of iron-based catalysts is attractive due to their high FTS activity as well as their water–gas shift reactivity, which helps make up the deficit of H_2 in the syngas from modern energy-efficient coal gasifiers (1). The catalyst for the slurry bubble column reactor is precipitated iron oxide which is spray-dried to yield particles with diameters of 30–70 μm. One major limitation of iron-based catalysts is that they tend to undergo attrition during use, as has been described in previous work from our laboratory (2–5). Therefore, a catalyst support/binder is an essential structural additive for iron-based FTS catalysts to improve catalyst attrition resistance and the aging characteristics of the catalyst. Many advantages of supported iron catalysts, such as improved catalyst stability, decreased deactivation rate, and improved selectivity, have been reported in previous work (6–8). Nevertheless, catalysts containing a binder or support usually suffer from lowered FTS activity both in the fixed-bed reactors (7) and in the slurry reactors (8).

The lower activity of supported Fe catalysts has been attributed to the effect of metal–support interactions (6–8) that affect the reducibility of the iron phase. The objective of this work was to investigate the nature of these metal–support interactions. It has been proposed that an FeO phase is stabilized on the support, while no such phase is seen in unsupported catalysts (9–11). In the work of Boudart *et al.* (9), the existence of an FeO–MgO phase was based on X-ray diffraction and Mössbauer spectroscopy. Kock *et al.* (10) inferred the presence of FeO on the basis of a decrease in the saturation magnetization of the Fe/MgO or Fe/γ-Al_2O_3 catalysts after reduction beyond 645 K when Fe_3O_4 starts to transform into FeO. It was reasoned that if either an α-Fe or Fe_xC carbide phase had formed, there would have been an increase in magnetization upon further reduction. One problem with any analysis based on magnetic properties or from X-ray diffraction is the dependence on particle size. It is known that small particles of α-Fe below 6 nm show superparamagnetic behavior, making them difficult to detect in zero-field Mössbauer spectra at room temperature (11). Small α-Fe particles yield a doublet that is similar to that obtained from Fe^{2+} at room temperature. It is only after application of a strong magnetic field that these two species can be resolved. Furthermore, XRD is not sensitive to dispersed phases due to excessive peak broadening and both Mössbauer and XRD suffer from lack of spatial resolution.

[1] Present address: Conoco Inc., Ponca City, OK 74602.
[2] To whom correspondence should be addressed. Fax: (505) 277-1024. E-mail: datye@unm.edu.

0021-9517/00 $35.00

Fe catalysts during FTS contain multiple phases with differing size and morphology. Detailed localized information about phase distribution and phase evolution will be helpful in understanding the nature of the metal–support interaction, especially for multicomponent systems. The most commonly used method to study catalyst reducibility and metal–support interactions is temperature-programmed reduction (TPR). However, many factors influence the location of peaks during TPR, making the assignment of TPR peaks difficult. A suitable method to follow phase transformations accompanying the TPR process is essential. In this work we have used high-resolution transmission electron microscopy (HRTEM) to follow the phase transformations during TPR. As demonstrated recently, HRTEM can be successfully used to identify different kinds of iron carbides in working iron FTS catalysts removed from slurry reactors (12, 13). Recent activation studies (14, 15) on unsupported iron catalysts show that CO activation can lead to high-activity iron catalysts. Since the formation of iron carbides appears to be essential for development of high FTS activity, the reducibility under CO environments is most relevant for evaluating the effects of iron–support interactions on Fischer–Tropsch reactivity.

In a previous study (10), the authors came to the surprising conclusion that iron carbide did not form when Fe/γ-Al_2O_3 was reduced in CO while θ-carbide formed at these temperatures on an unsupported Fe catalyst. To examine the role of the support, we have contrasted the behavior of two catalysts: a model catalyst where Fe was supported on Stöber silica microspheres, and an unsupported catalyst previously used in slurry bubble column reactor tests. High-resolution transmission electron microscopy (HRTEM) and XRD were used to monitor iron phase evolution during CO-TPR and H_2-TPR. The specific objective was to follow phase changes in iron species during the reduction process, and to evaluate the possible formation of interfacial phases as a possible cause of metal–support interactions.

EXPERIMENTAL

Catalyst Preparation

Two catalyst samples were studied in this work. The unsupported catalyst was prepared by United Catalysts Inc. for the U.S. Department of Energy (DOE) by precipitation and spray drying. The nominal composition was 88.95 wt% Fe_2O_3, 11 wt% CuO, and 0.05 wt% K_2O (3). The supported catalyst was prepared by incipient wetness impregnation. In order to simplify analysis for TEM, we used 270-nm-diameter nonporous Stöber silica spheres (16) as a model support. While this is not a typical support used in industry, the simple geometry of this support facilitates TEM analysis and allows us to see the formation of interfacial phases, if any. The precursors ($Fe(NO_3)_3$, $Cu(NO_3)_2$, K_2CO_3) were mixed in an aqueous solution and allowed to contact the silica support. The mixture was evaporated to dryness in a rotary evaporator at around 80°C. The sample was then dried in an oven overnight at 100°C. The composition of this as-prepared catalyst was 20.0 wt% Fe, 0.9 wt% Cu, and 1.1 wt% K as measured by atomic absorption (AA) spectroscopy. Aliquots of the catalyst samples were calcined in air at 300°C, 430°C, and 500°C for 1 h each before being subjected to TPR experiments. After the TPR run was complete, these samples were reoxidized with 5% O_2 in helium at a temperature ramp of 10°C min to 500°C and held at that temperature for 1 h.

Temperature-Programmed Reduction (TPR)

The temperature-programmed reduction experiments were performed in a conventional atmospheric quartz flow reactor (3 mm i.d.). A flow of 10% CO in He or 10% H_2 in Ar, maintained at a flow rate of 20 sccm, was used as the reducing gas. CO or H_2 consumption was monitored by measurement of the thermal conductivity (TC) of the effluent gas on a Varian 3400 GC. An in-line ascarite (in the CO-TPR mode) or drierite (in the H_2-TPR mode) trap, located between the reactor and the thermal conductivity detector, was used to continuously remove carbon dioxide or water produced during reduction. Typically, a 20–30-mg catalyst bed was mounted in the U-shaped quartz reactor and was precalcined *in situ*. In all the TPR runs, a ramp of 10°C/min was used. After the first TPR, the sample was purged with He, cooled to room temperature in He, and reoxidized by temperature-programmed oxidation in a flow of 5% O_2 in He using a temperature ramp of 10°C/min. The second run TPR was then performed for the reoxidized catalyst sample. The temperature at the peak maximum (T_{max}) and the temperature at the peak onset (T_{onset}) in TPR profiles were used as measures of the reducibilty of these iron catalysts.

Transmission Electron Microscopy (TEM) Measurements

In order to identify each peak in the TPR profiles, the TPR run was repeated under conditions identical to the first run, but after the TPR peak of interest, the run was aborted by switching the reducing gas flow to helium. The sample was purged with helium at that temperature for 30 min, and then cooled to room temperature. The sample was carefully passivated and collected for TEM and XRD measurements. TEM measurements were performed on a JEOL 2010 HRTEM with a point resolution of 1.9 Å. In order to avoid possible contamination, the sample powder was directly mounted on the TEM grid without using any solvent.

X-Ray Powder Diffraction (XRD) and BET Surface Area Measurements

The XRD measurements were carried out on a Scintag PAD-V powder X-ray diffractometer, equipped with a

TABLE 1

BET Surface Area of Iron Catalysts under Different Treatments

Sample	Treatment	BET area (m^2/g)
UCI unsupported catalyst	As received	36
	300°C, 1 h	35
	300°C, 5 h	8
	500°C, 1 h	15
	CO-TPR to 320°C	22
	CO-TPR to 500°C	6
Stöber silica spheres	As prepared	9
Supported catalyst	As prepared	24
	CO-TPR to 300°C	22
	CO-TPR to 500°C	21

Cu$K\alpha$ source. All diffraction patterns were recorded in the step-scan mode with a step size of 0.04 deg/step and a scan rate of 0.4 deg/min. The BET surface areas of catalysts were determined via nitrogen adsorption, using a Micromeritics Gemini 2360 surface area analyzer. Before each measurement, the sample was purged with UHP nitrogen at 120°C overnight. Results of BET surface area measurements for the iron catalysts after different treatments are listed in Table 1.

TPR Quantitation

The TPR profiles are quantified by integrating the peak areas. In many cases, the TPR peaks corresponding to transformations of $CuO \rightarrow Cu$ and $Fe_2O_3 \rightarrow Fe_3O_4$ were found to overlap. Therefore, the combined area of these peaks was used for comparison. Table 2 gives relative amounts of the calculated and measured CO and H_2 uptakes for the reduction of magnetite to α-Fe or to iron carbide compared to the area of the first set of peaks ($CuO \rightarrow Cu + Fe_2O_3 \rightarrow Fe_3O_4$) during CO-TPR and H_2-TPR.

TABLE 2

Ratio of TPR Peak Area for the Magnetite Reduction Peak to the Sum of the Peak Areas for Reduction of CuO → Cu and Hematite → Magnetite

Sample	Peak area ratio
UCI catalyst (calculated)	4.5
UCI H_2-TPR, 1st (300°C calcined)	4.0
UCI H_2-TPR, 1st (500°C calcined)	4.4
UCI H_2-TPR, 2nd	3.7
UCI CO-TPR, 1st	5.6
Supported catalyst (calculated)	6.0
Supported H_2-TPR, 1st (300°C calcined)	6.7
Supported H_2-TPR, 1st (500°C calcined)	6.9
Supported H_2-TPR, 2nd	5.4
Supported CO-TPR, 1st (as prepared)	19.8

Note. The first row shows the calculated uptake ratio.

RESULTS AND DISCUSSION

H_2-TPR of the Unsupported Iron Catalyst

Figure 1 shows the H_2-TPR profiles of the unsupported catalyst after being calcined in air at (a) 300°C, (b) 430°C, and (c) 500°C for 1 h, respectively. Curve d is the second-run H_2-TPR profile of the same sample as that in (a) after oxidation at 500°C. Samples collected for XRD and TEM measurements were indicated on these TPR profiles by arrows. For a, b, and c in Fig. 1, the first peak is broad and appears to represent several overlapping peaks. Both TEM and XRD measurements (not shown here) indicate that crystalline Cu metal and Fe_3O_4 are the only phases present in samples removed after the first set of overlapped peaks. This implies that these overlapped peaks can be related to the phase transformations: $CuO \rightarrow Cu$ and $Fe_2O_3 \rightarrow Fe_3O_4$. The last broad peak on the TPR profile corresponds to the phase transformation of $Fe_3O_4 \rightarrow \alpha$-Fe as confirmed by XRD. The large peak width for the $Fe_3O_4 \rightarrow \alpha$-Fe transformation indicates this is slow process, which is consistent with the literature (14).

Figure 1 shows also how the catalyst pretreatment influences TPR peak positions. The first overlapped set of peaks becomes better defined with increasing calcination temperature (curves a, b, and c). When the catalyst was subjected to 500°C oxidation after the first TPR and a second-run TPR was performed (curve d), the nature of the first peak changes significantly. The broad peak seen in Fig. 1a has been replaced by a smaller peak at the same position and a new peak that is symmetrical occurs at a higher temperature. The large peak representing the $Fe_3O_4 \rightarrow \alpha$-Fe phase transformation seems to be unaffected by any of these pretreatments. Oxidation of the sample after the

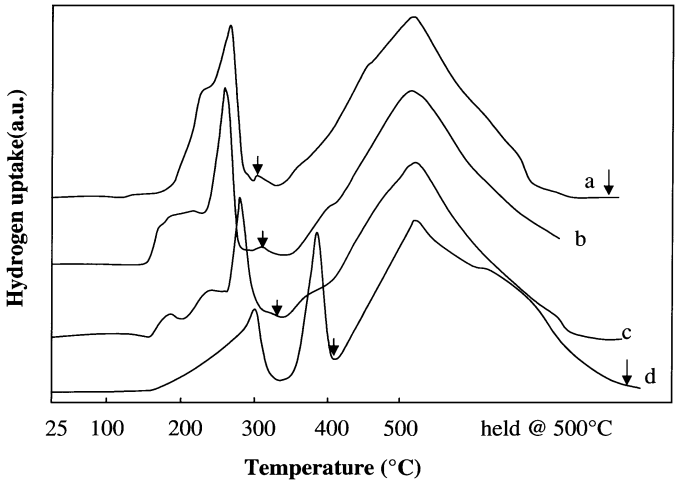

FIG. 1. Precalcination effects on the H_2-TPR profile for the unsupported catalyst. Arrows show where samples were removed for microstructural analysis: (a) 300°C × 1 h, (b) 430°C × 1 h, (c) 500°C × 1 h, (d) second run after completion of run (a) and catalyst reoxidation at 500°C.

first TPR (curve d) therefore does not affect the nature of the $Fe_3O_4 \rightarrow \alpha$-Fe phase transformation. However, the $CuO \rightarrow Cu$ and $Fe_2O_3 \rightarrow Fe_3O_4$ phase transformation temperatures are affected by calcination and oxidation as discussed below.

Reduction of iron oxides in hydrogen (H_2-TPR) of both unpromoted and Cu-promoted catalysts has been reported (10, 17, 18). It was found that in the promoted catalyst, the reduction of Fe_2O_3 occurred simultaneously with the CuO at atomic ratios of Fe : Cu up to 60 : 40 (18). At higher ratios, two distinct peaks could be seen, one near the CuO–Cu reduction temperature and the other at a higher temperature corresponding to the reduction of unpromoted Fe_2O_3. The promotional effect of Cu was attributed to its ability to dissociate H_2 and provide a source of atomic H to assist in the reduction of Fe_2O_3. In our TPR data, we see a set of overlapped peaks at calcination temperatures up to 500°C. This implies that the CuO is well mixed with the Fe_2O_3 phase. No separate CuO diffraction peaks can be seen in this the fresh sample by XRD. After TPR and oxidation, in the second-run TPR, we now see two distinct peaks (curve d). The first of these peaks is broad and looks very similar to the first peak seen in curves a–c. The second peak is more symmetrical and occurs at higher temperatures. We attribute the first peak to the reduction of a mixed CuO–Fe_2O_3 phase while the second one represents Fe_2O_3 that has phase segregated. This phase segregation must occur during the first reduction since XRD of the catalyst after the first TPR (not shown) indicates the presence of well-defined Cu metal and Fe metal peaks. After oxidation, the Cu and Fe oxides must remain segregated; hence the reduction peaks for the Fe oxides shift to higher temperatures. It therefore appears that for CuO to serve as a promoter, intimate contact with the iron oxides is essential.

H_2-TPR of the Supported Iron Catalyst

Figure 2 shows the H_2-TPR profiles of the supported catalyst. Three peaks are present in the TPR profiles. Curve a corresponds to the first run which was performed after a 300°C calcination. Curve b represents the second run after a 500°C oxidation at the end of the first run. Curve c is a TPR profile of supported copper oxide. Since the first two peaks are close to each other, we could not collect catalyst samples after the first peak in the TPR profiles a and b. After the second peak, both TEM and XRD show that the iron oxide has been reduced to magnetite. Due to the small amount of Cu present in the supported catalyst, no distinct Cu metal peak could be detected by X-ray or electron diffraction. Figure 3a shows a low-magnification view of an iron-rich region in the catalyst collected after the TPR run to 314°C. The inset diffraction pattern conclusively shows that the iron phase is magnetite.

From the TPR profile we can see that the ratio of the area of the first TPR peak to that of the second one changed significantly after the first-run TPR. Since this sample contains 0.9 wt% copper compared to 20 wt% Fe, the calculated hydrogen uptake for $CuO \rightarrow Cu$ should be only one-third of that for Fe_2O_3 to Fe_3O_4 ($H \rightarrow M$). In fact, the first peak is larger than the second, which means we cannot attribute the first peak to the $CuO \rightarrow Cu$ reduction. The reduction temperature of a silica-supported copper oxide occurs at significantly lower temperature, $T_{onset} = 150$°C (Fig. 2c) compared with $T_{onset} = 180$°C for the first peak in Fig. 2a. The higher reduction temperature for the first peak compared to that for the $CuO \rightarrow Cu$ transformation indicates that copper is well mixed with iron. In agreement with the behavior of the unsupported catalyst we can suggest that the first peak represents reduction of CuO well mixed with Fe_2O_3, while the second peak corresponds to the $Fe_2O_3 \rightarrow Fe_3O_4$ reduction. In the second-run TPR profile, we can see that the ratio of the peak areas of the first two peaks has changed significantly. The second-run TPR shows increased separation between these two peaks, suggesting that some of the Cu may have segregated and is not able to facilitate the reduction of $Fe_2O_3 \rightarrow Fe_3O_4$. This segregation must occur during the first TPR when the iron oxide is reduced to metallic Fe.

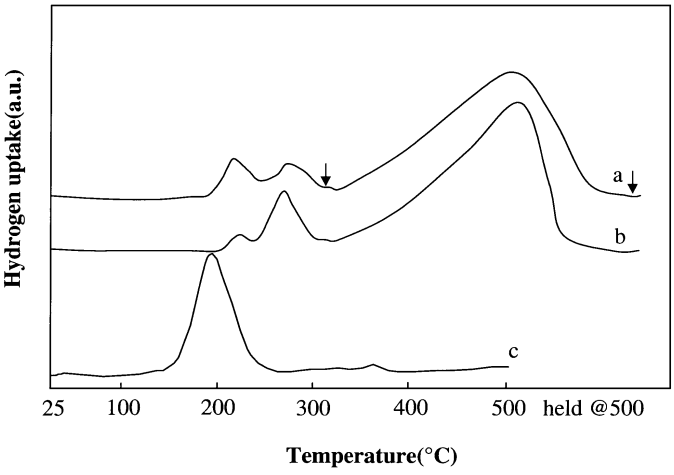

FIG. 2. H_2-TPR profiles of Fe-supported iron catalysts: (a) Fe/SiO_2 first run, (b) Fe/SiO_2 second run, and (c) 10 wt% Cu/SiO_2.

The last broad peak corresponds to the transformation of magnetite to α-Fe. Figure 3b is a typical TEM image at low magnification showing the morphology of the catalyst after the complete H_2-TPR run. The porous morphology of the iron oxide is now lost and instead we now see dense metallic particles of α-Fe.

All the characterization methods used in this study, TPR (Table 2), XRD, and TEM, demonstrate that the as-prepared supported iron catalyst is reducible to α-Fe after a complete H_2-TPR. This conclusion is based on the absence of diffraction due to crystalline silicate phases or to the suboxide FeO. While previous work (9, 10) has implied that iron supported on silica is harder to reduce, the

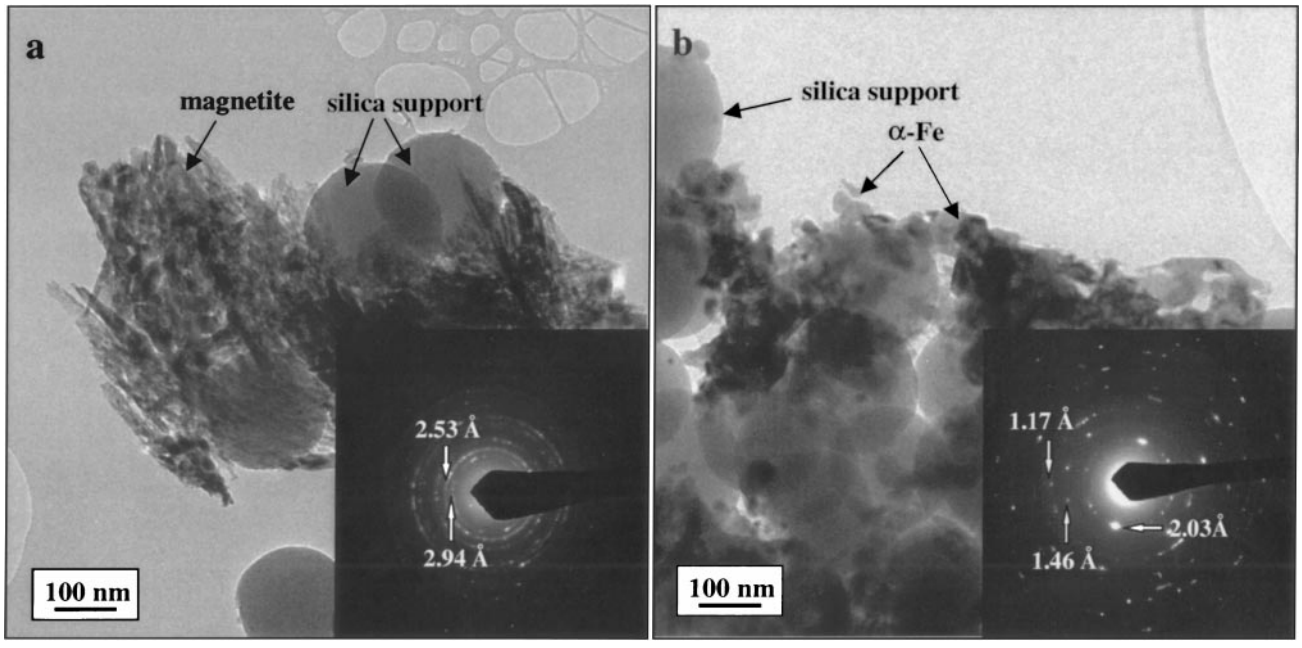

FIG. 3. TEM images of the Fe-supported catalyst during H_2-TPR: (a) after H_2–TPR to 314°C and (b) after a complete run to 500°C.

presence of Cu helps achieve complete reduction. An SMSI-like decoration has also been suggested as a possible mechanism for the interaction mechanism for silica-supported iron oxide (10). We are uniquely equipped to address this latter mechanism since we used nonporous Stöber silica microspheres as support. The nonporous silica permits imaging of the metal surfaces and metal–support interfaces. Figure 4 is a typical high-magnification image of an edge-on metal particle. We can see a metal particle of iron surrounded by a layer about 3 nm thick that shows a lighter contrast. We have shown in previous work (23) that this surface layer is magnetite formed during the passivation of the reduced catalyst before it is removed from the microreactor and exposed to air. The thickness of this layer depends critically on the passivation conditions. While the magnetite is amorphous since it is formed at room temperature, exposure to the electron beam during high-magnification imaging in the TEM causes crystallization, upon which we can confirm that it represents polycrystalline magnetite. Besides the α-Fe and Fe_3O_4 phases shown in this image, we do not see any evidence for an Fe–silica interfacial phase.

Comparing with previous work (10, 17), where an interfacial phase was implicated, we can point out that a high-surface-area silica support was used and iron oxide was made by precipitation (FeOOH was actually the precursor). In our study, the precursor hematite was made by the decomposition of impregnated iron nitrate. Furthermore, by using nonporous silica spheres as the model support, we have eliminated all pores and hence the diffusion of product water vapor is facilitated, minimizing formation of hydrosilicates.

CO-TPR of the Unsupported Fe Catalyst

CO-TPR profiles of the unsupported iron catalyst after calcination at (a) 300°C and (b) 500°C are shown in Fig. 5. The other two curves in this figure show the TPR after a 500°C oxidation performed after the TPR run (a), curve c, and the CO-TPR of the Cu/SiO_2 catalyst, curve d. The TPR shows a three-peak pattern, but the peaks are better separated than in the H_2-TPR experiment, allowing us to collect samples after each peak. The first peak must correspond to the CuO to Cu ($CuO \rightarrow Cu$) phase transformation since it occurs at temperatures where the reduction peak is seen on CuO/SiO_2 (Fig. 5d). No crystalline Cu metal phase could be detected after the first peak via XRD analysis (not shown). After the first peak (curve b) XRD showed hematite as the only crystalline phase detected. It is possible that the low reduction temperature (200°C) does not allow Cu to crystallize and form metal particles that can be detected by XRD.

The second peak represents the Fe_2O_3 to Fe_3O_4 ($H \rightarrow M$) transformation based on TEM analysis. Results of TEM examination of the catalyst samples after the first peak (curve a) are shown in Fig. 7a. This sample was collected after CO-TPR to 294°C. The inset high-resolution image shows the (220) lattice fringes of magnetite. The BET surface area was measured on a sample where the CO reduction had been carried out to 320°C (Table 1). The BET surface areas had dropped from 36 m^2/g to 22 m^2/g.

No evidence of carbide formation was found for this unsupported iron sample according to XRD (Fig. 6) and also TEM (Fig. 7). After the first complete CO-TPR run, the

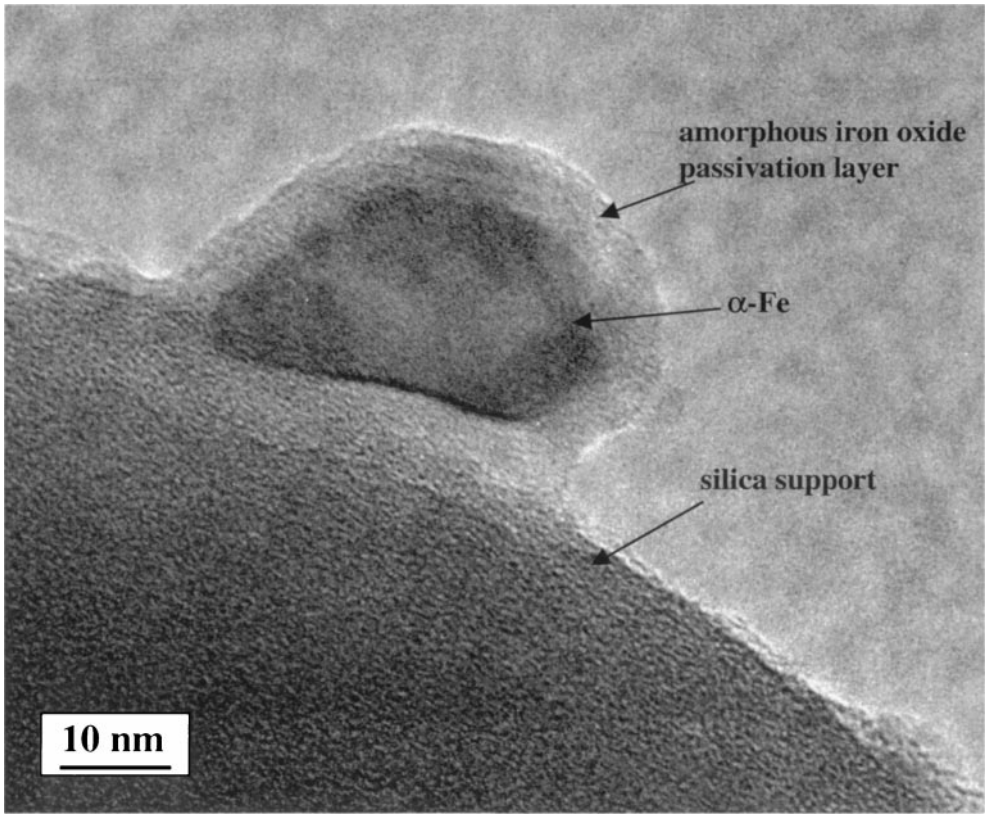

FIG. 4. Higher manification image of the supported catalyst after a complete H_2-TPR run to 500°C.

magnetite has been almost completely transformed to α-Fe with only a very small amount of unreduced magnetite left behind (Fig. 5a). Figure 7b shows that dense α-Fe particles coexist with some unreduced magnetite particles, which is consistent with the low surface area, and the X-ray diffraction powder profile. For the second-run CO-TPR, it took a very long time for the TPR peak of M → α-Fe to go back to the baseline. The XRD pattern for the sample taken out of the reactor after the second-run CO-TPR and kept at 500°C for 30 min still shows a significant magnetite content. From the narrowing of the peak width, it is clear that all of these three phases, α-Fe, Cu, and magnetite, increased in crystal size after the first TPR run. The BET surface area measurement in Table 1 also shows evidence for considerable sintering, since the surface area of the unsupported catalyst dropped to 6 m^2/g after the complete CO-TPR run.

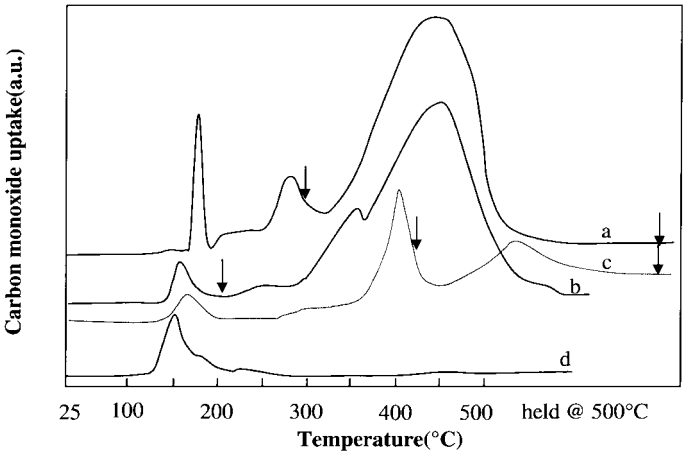

FIG. 5. Calcination effects on CO-TPR profiles for the UCI unsupported Fe catalyst: (a) 300°C × 1 h, (b) 500°C × 1 h, (c) second run after completion of run (a), and (d) 10 wt% Cu/SiO_2.

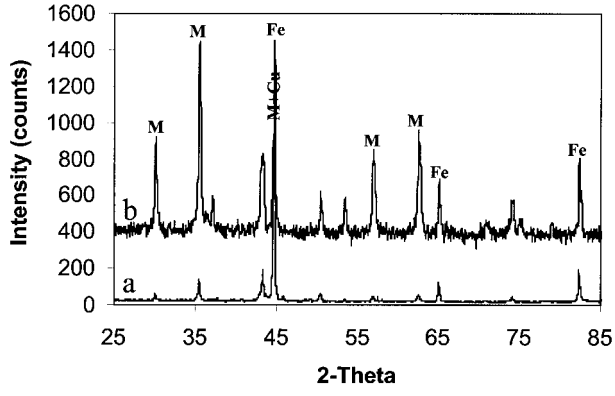

FIG. 6. XRD powder patterns of the UCI unsupported Fe catalyst during CO-TPR: (a) after the first TPR run to 500°C and (b) after the second TPR run.

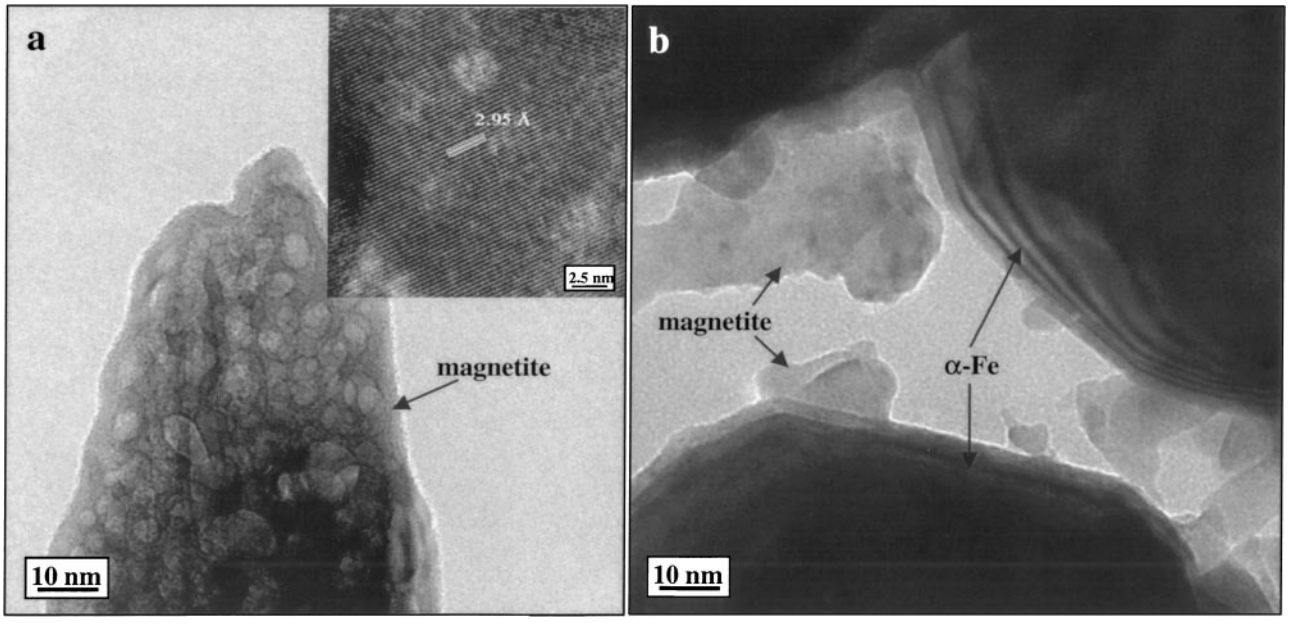

FIG. 7. TEM images of the unsupported iron catalyst in the course of CO-TPR: (a) after the H → M transformation peak (294°C) and (b) after a complete TPR run to 500°C.

Figure 5 shows that calcination causes a gradual broadening of the first peak and a systematic shift of the second peak toward higher temperature. The CuO → Cu and H → M peaks shift in opposite directions; i.e., the former shifts to lower temperature and the latter to higher temperature. Since growth of particle size could also contribute to a change in TPR profiles, XRD was used to check the hematite particle size change during calcination treatments. However, no significant changes in the peak broadening of the XRD peaks could be observed after calcination to 500°C for 1 h. Also, no separate CuO peak could be detected after calcination. There is, however, a drop in the BET surface area after calcination indicating a possible decrease in porosity. Calcination may also cause copper to segregate, and therefore not be able to facilitate the H → M transformation during TPR. These observations are consistent with the literature where it has been reported that copper (15) facilitates the CO reduction of iron oxide.

CO-TPR on the Supported Fe Catalyst

The supported Fe catalyst was also subjected to CO-TPR using conditions similar to those used for the unsupported catalyst. As shown in Fig. 8, this catalyst also shows a three-peak pattern. The very first small peak shifts to higher temperature with increasing calcination temperature. However, the other two peaks do not show a significant change with increasing calcination temperature, even for the second-run TPR. Except for the peak shift of the first small peak, the second-run CO-TPR profile looks almost identical to the first-run profile. These results mean that the iron deposited on the Stöber silica spheres is quite stable to the reduction–oxidation treatments, and sintering of iron particles does not occur in the supported catalyst.

The supported catalyst contains only 0.9 wt% copper. The calculated CO uptake for CuO → Cu is one-third of that for H → M. From results of the CO-TPR of the unsupported catalyst, we would expect the CuO → Cu transformation to occur below 200°C (Fig. 5). No peak is seen around this temperature, probably because of the small amount of Cu in the supported catalyst. We attribute the first peak at 225°C to the H → M transformation. The second peak in the CO-TPR of the supported catalyst can be related to the phase transformations from magnetite to χ-carbide (M → χ) as

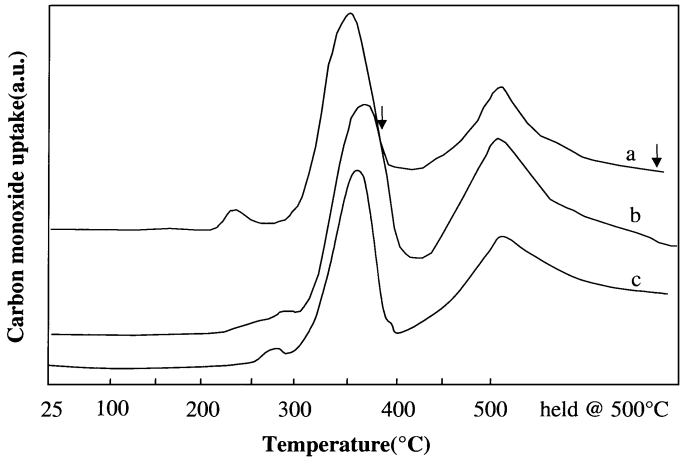

FIG. 8. CO–TPR profiles of Fe-supported catalyst (a) as prepared, (b) calcined at 500°C for 1 h, and (c) second run CO-TPR after run (a).

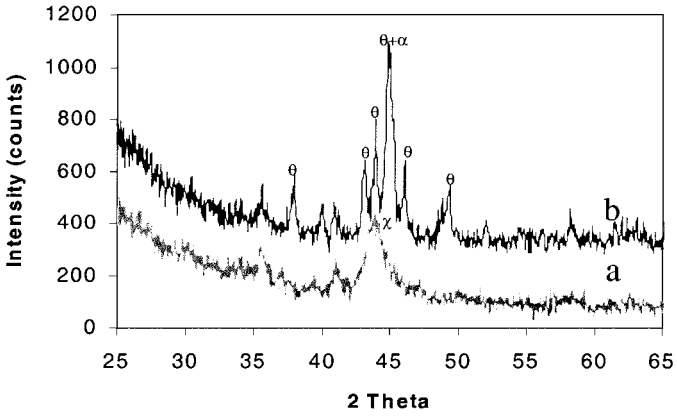

FIG. 9. XRD powder patterns of the supported Fe catalyst during CO-TPR: (a) after CO-TPR to 380°C and (b) after the complete TPR run to 500°C.

described below. The XRD spectrum in Fig. 9a is the diffraction pattern of the supported catalyst sample taken after the first CO-TPR run to 380°C (right after the second peak in the CO-TPR profile). This diffraction pattern, which shows a major broad peak with the maximum at 2θ of 43.6°, is similar to that of Fe carbides formed under relatively low-temperature (190–240°C) FT synthesis conditions (19). According to both Mössbauer and XRD (19) analysis, this pattern corresponds to a mixture of Fe carbide phases (ε and χ): with increasing reaction temperature, the peak shifts to higher 2θ accompanying a phase transformation of ε to χ (19, 20). By comparing the peak maximum with that of Ref. (19), the carbide phase formed here should be mostly χ carbide. This assignment is also confirmed by results of electron diffraction and high-resolution TEM analysis as will be shown later in this section.

Figure 9b represents a diffraction pattern for the sample after the complete CO-TPR run. This pattern shows the presence of cementite (Fe_3C) together with α-Fe. Therefore, from 380°C to 500°C, some of the χ-$Fe_{2.5}C$ carbide transformed to cementite ($\chi \rightarrow \theta$) and some χ-carbide transformed to iron metal ($\chi \rightarrow \alpha$-Fe). This is understandable because cementite is the stable carbide phase at high temperature (20). Since neither of these two phase transformations involves consumption of carbon, the high-temperature peaks in the CO-TPR profiles of the supported catalyst simply correspond to carbon deposition, as confirmed by TEM below.

As shown in Table 2, the measured CO uptake matches the calculated CO uptake very well for the unsupported iron catalyst. However, the agreement is much poorer for the supported Fe catalyst: the measured ratio of CO uptakes ($M \rightarrow \chi$) is 3.3 times greater than the calculated value. The large amount of CO uptake in the 380°C to 500°C region corresponds to carbon deposition on the catalyst. We have noticed that the CO-TPR curves do not go back to the baseline at the end of the TPR where we hold the temperature at 500°C. The additional CO uptake during phase transformations of $M \rightarrow \chi$ and $\chi \rightarrow \theta$, α-Fe indicates that the Boudouard reaction, which leads to carbon deposition, accompanies these phase transformations.

Figure 10 shows TEM images of the supported iron catalyst collected after CO-TPR to 380°C. The low-magnification view in Fig. 10a shows that the iron oxide platelets have been transformed to smaller particles. The

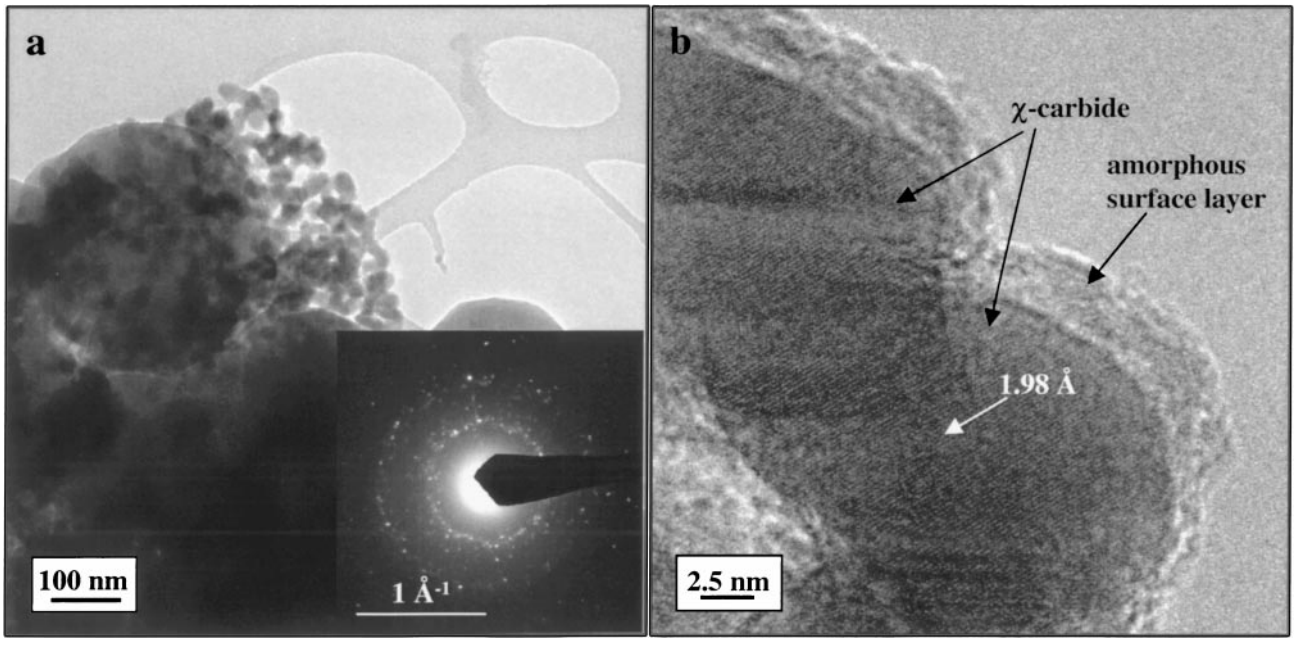

FIG. 10. TEM images of the supported Fe catalyst after CO-TPR to 380°C. The diffraction pattern and lattice fringes confirm the presence of χ-carbide: (a) low-magnification view and (b) high-magnification showing carbide structure and an amorphous surface layer.

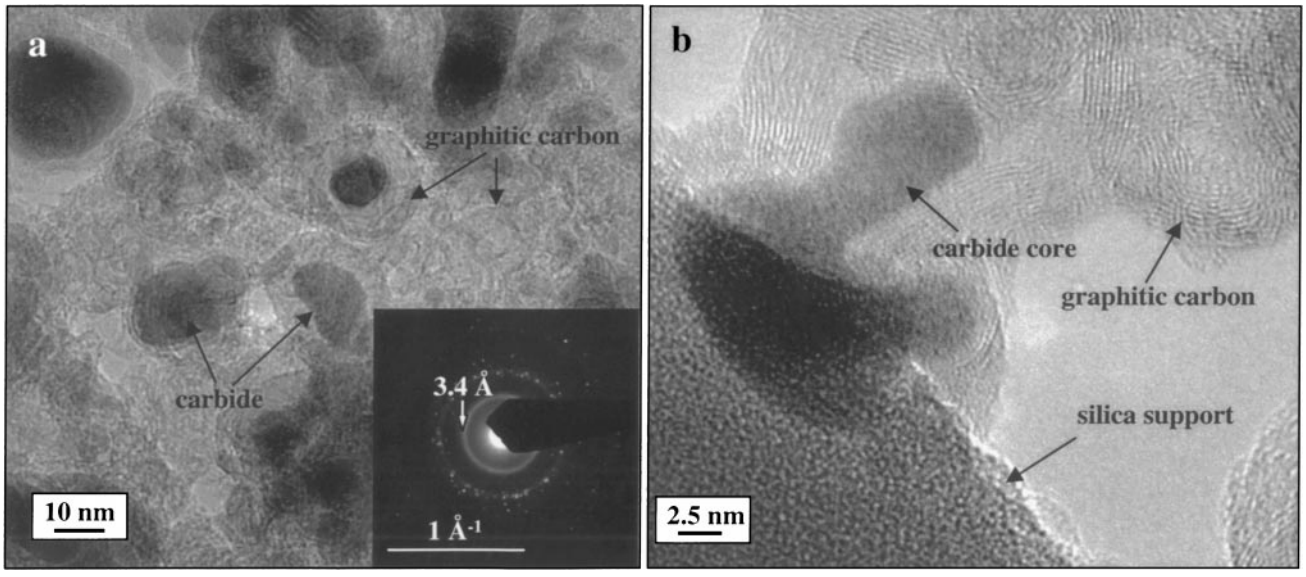

FIG. 11. TEM images of the supported Fe catalyst after a complete CO-TPR run: (a) a view of an iron-rich area and (b) HRTEM of a single carbide particle.

electron diffraction pattern reveals a very complicated pattern. The diffuse spots around 2 Å are consistent with the multiple reflections for the χ-carbide phase (21, 22). The high-resolution image in Fig. 10b shows lattice fringes of 1.98 Å corresponding to the *d*-value of the $(\bar{5}\bar{1}1)$ plane of χ-carbide. At high magnification, it can be seen that the χ-carbide particles are all surrounded with an amorphous surface layer of a thickness of around 2–3 nm, which is typically seen in iron catalysts after normal Fischer-Tropsch synthesis or activation treatments with CO or syngas (3). Electron energy-loss spectroscopy (EELS) analysis shows that this amorphous layer is carbonaceous in nature (23) and not a passivation film of magnetite which is expected when a reduced Fe surface is exposed to air (24). The morphology of the sample after CO-TPR to 500°C is quite different. Carbon deposition in the form of graphite can be seen everywhere in the sample, covering the iron carbide particles. The size of iron carbide particles also varies significantly from a few to tens of nanometers. Figure 11a is a TEM image taken from an iron-rich region. The inset diffraction pattern shows a typical diffuse spot pattern for iron carbide. The θ-carbide (cementite) particles have irregular shapes and the particles are covered by graphitic carbon.

Role of the Silica Support on Phase Transformations in the Fe Catalyst

This study shows clearly some of the support effects during reduction of the iron catalyst in CO. The most important effect of the silica support is an improvement in the thermal stability of the Fe catalysts. The unsupported catalyst loses surface area upon calcination; therefore, the second TPR run is very different from the first one. A comparison of the first-run H_2-TPR with the second-run H_2-TPR (Fig. 2) shows that the silica support is very effective at inhibiting the sintering of the iron catalyst. One concern with the silica support is the possible presence of an interfacial phase, which could inhibit the reducibility of the Fe oxide. This study found no evidence for any interfacial phase at the iron–support interface, and the reducibility of the iron oxide phases seems to be similar to that of the unsupported catalyst.

One significant effect of the support was on the phase transformations of the Fe catalysts in CO. We found that the unsupported catalyst could only be reduced to iron metal while the supported catalyst transformed easily into the iron carbide. The behavior of the unsupported catalyst is very unusual and we feel that this difference in the extent of carburization is caused by the presence of trace amounts of S in the unsupported catalyst. Since the unsupported catalyst was prepared on an industrial scale, the precursors may be contaminated with small amounts of S. In previous work with this same catalyst (25), we found that the S was seen by Auger electron spectroscopy on the catalyst surface only when the iron oxide was reduced completely to metallic Fe. Once the iron oxide was reduced to metallic Fe, it was not possible to further transform it into iron carbide. On the other hand, if the unsupported catalyst was directly carbided at a low temperature directly from its oxide state, it was possible to completely transform it into the iron carbide (3). This finding is consistent with recent work by Bromfield and Coville (26) where it was shown that the presence of $(SO_4)^{2-}$ was not detrimental to catalyst performance, but S^{2-} severely inhibited catalyst activity. We

therefore feel that during TPR in CO, the rapid increase in temperature leads to conditions where the residual S impurities accumulate on the surface of the catalyst, inhibiting the transformation into iron carbide.

The TPR results reported here also shed light on another aspect of Fe catalysts, whether a distinct phase transformation from iron oxide into metallic iron is seen before the catalyst transforms into iron carbide. Our results show that for the supported catalyst, we see no distinct peaks that could be assigned to the transformation of magnetite into α-Fe. It appears that these two steps happen simultaneously during the course of CO-TPR on the supported catalyst. On the other hand, in the unsupported catalyst, the presence of S impurities inhibits the dissociation of CO, so we see no carbiding of the α-Fe as well as no deposition of amorphous carbon on the catalyst.

Effect of Copper on the Phase Transformations of Iron

It has been recognized (6) that copper promotes the reduction of hematite to magnetite, and also the reduction of magnetite to α-Fe to a lesser extent (14). A suggested mechanism for this promotion effect is the migration of atomic hydrogen from reduced Cu sites to the iron oxide (10). A major difference between the H_2 and CO-TPR is the simultaneous reduction of copper and iron oxides in H_2, whereas in CO the copper oxide seems to reduce first followed by the iron phase. Nonetheless, there is a clear promotion by the Cu also during CO-TPR. Therefore, the copper needs to be very well mixed with iron oxide to provide the most favorable promoter effect on the H → M phase transformation. Calcination seems to cause segregation of the copper and iron oxides leading to shifts in the reduction peak temperatures of the iron to higher temperatures. The major differences between the first and second TPR runs can also be related to the segregation of the Cu and Fe phases. It appears, therefore, that to prevent segregation, high-temperature calcination treatment of iron catalyst precursors should be avoided.

CONCLUSIONS

In H_2-TPR, both the supported and the unsupported Fe catalysts were reduced to iron metal. No iron–support interfacial phase could be detected by TEM and it appears that the iron phase is completely reducible. Most importantly, the silica support significantly lowers the mobility of iron phases to avoid sintering during the TPR runs. As a result, iron particles do not grow significantly, and we did not see dramatic changes in reducibility of the supported Fe catalyst during the reduction–oxidation treatments. During CO-TPR of the unsupported catalyst, sintering of reduced iron particles dominates over carburization. The unsupported Fe catalyst is only reduced to iron metal due to the presence of S impurities present in this catalyst. Copper acts as an important promoter for reduction of iron oxide in both H_2-TPR and CO-TPR. For the unsupported iron catalyst, calcination appears to cause copper segregation from iron phases and results in the loss of promotion effects.

ACKNOWLEDGMENTS

We acknowledge support of this research by the U.S. Department of Energy University Coal Research Grant DE-FG22-95PC95210 and DE-FG26-98FT40110. Electron microscopy was performed at the Microbeam Analysis Facility within the Department of Earth and Planetary Sciences, University of New Mexico, which is supported by the NSF, NASA and the State of New Mexico.

REFERENCES

1. Rao, V. U. S., Stiegel, G. J., Cinquergrane, G. J., and Srivastava, R. D., *Fuel Processing Technol.* **30**, 83 (1992).
2. Datye, A. K., Shroff, M. D., Jin, Y., Brooks, R. P., Wilder, J. A., Harrington, M. S., Sault, A. G., and Jackson, N. B., *Stud. Surf. Sci. Catal.* **101**, 1421 (1996).
3. Shroff, M. D., Kalakkad, D. S., Coulter, K. E., Kohler, S. D., Harrington, M. S., Jackson, N. B., Sault, A. G., and Datye, A. K., *J. Catal.* **156**, 185 (1995).
4. Kalakkad, D. S., Shroff, M. D., Kolher, K. E., Jackson, N. B., and Datye, A. K., *Appl. Catal. A: General* **133**, 335 (1995).
5. Pham, H. N., Reardon, J., and Datye, A. K., *Powder Technol.* **103**, 95 (1999).
6. Dry, M., *in* "Catalysis—Science and Technology" (J. R. Anderson and M. Boudart, Eds.), Vol. 1, p. 160. Springer, New York, 1981.
7. Bukur, D. B., Lang, X., Mukesh, D., Zimmerman, W. H., Rosynek, M. P., and Li, C., *Ind. Eng. Chem. Res.* **29**, 1588 (1990).
8. Bukur, D. B., "Development of Improved Iron Fischer–Tropsch Catalysts," Technical Report DOE/PC/89868, February, 1994.
9. Boudart, M., Delbouille, A., Dumesic, J. A., Khammouma, S., and Topsøe, H., *J. Catal.* **37**, 486 (1975).
10. Kock, A. J. H. M., Fortuin, H. M., and Geus, J. W., *J. Catal.* **96**, 261 (1985).
11. Clausen, B. S., Topsøe, H., and Morup, S., *Appl. Catal.* **48**, 327 (1989).
12. Jin, Y., and Datye, A. K., *Proc. Int. Congr. Electron Microsc. 1998* **2**, 379 (1998).
13. Jin, Y., and Datye, A. K., *Natural Gas Coversion V, Stud. Surf. Sci. Catal.* **119**, 209 (1998).
14. Bukur, D. B., Okabe, K., Rosynek, M. P., Li, C. P., Wang, D. J., Rao, K. R. P. M., and Huffman, G. P., *J. Catal.* **155**, 353 (1995).
15. O'Brien, R. J., Xu, L., Spicer, R. L., Bao, S., Milburn, D. R., and Davis, B. H., *Catal. Today* **101**, 1 (1997).
16. Stöber, W., Fink, A., and Bohn, E. J., *J. Colloid Interface Sci.* **26**, 62 (1968).
17. Wielers, A. F. H., Kock, A. J. H. M., Hop, C. E. C. A., Geus, J. W., and van der Kraan, A. M., *J. Catal.* **117**, 1 (1989).
18. Wielers, A. F. H., Hop, C. E. C. A., Van Beijnum, J., Van der Kraan, A. M., and Geus, J. W., *J. Catal.* **121**, 364 (1990).
19. Niemantsverdriet, J. W., van der Kraan, A. M., van Dijk, W. L., and van der Baan, H. S., *J. Phys. Chem.* **84**, 3363 (1980).
20. Hofer, L. J. E., Cohn, E. M., and Peebles, W. C., *J. Am. Chem. Soc.* **71**, 189–195 (1949).
21. Dirand, M., and Afqir, L., *Acta Metall.* **31**, 1089 (1983).
22. Senateur, J. P., *Ann. Chim.* **2**, 103 (1967).
23. Jin, Y., Xu, H., and Datye, A. K., in preparation.
24. Shroff, M., and Datye, A. K., *Catal. Lett.* **37**, 101 (1996).
25. Datye, A. K., Shroff, M. D., Harrington, M. S., Sault, A. G., and Jackson, N. B., *Stud. Surf. Sci. Catal.* **107**, 169 (1997).
26. Bromfield, T. C., and Coville, N. J., *Appl. Catal.* **186**, 297 (1999).